# Accepted Manuscript


Infinite element in meshless approaches

P.H. Wen, J.J. Yang, T. Huang, J.L. Zheng, Y.J. Deng

PII: S0997-7538(17)30745-3

DOI: 10.1016/j.euromechsol.2018.05.010

Reference: EJMSOL 3610

To appear in: *European Journal of Mechanics / A Solids*

Received Date: 2 October 2017

Revised Date: 9 May 2018

Accepted Date: 11 May 2018

Please cite this article as: Wen, P.H., Yang, J.J., Huang, T., Zheng, J.L., Deng, Y.J., Infinite element in meshless approaches, *European Journal of Mechanics / A Solids* (2018), doi: 10.1016/j.euromechsol.2018.05.010.

# Infinite element in meshless approaches

P.H. Wen[1*], J.J. Yang[2], T. Huang[2] , J.L. Zheng[2] and Y.J. Deng[3]

[1]*School of Engineering and Materials Science, Queen Mary, University of London, London E1 4NS, UK*

[2]*School of Communication and Transportation Engineering, Changsha University of Science and Technology, Changsha, 410004, China*

[3]*School of Mathematics and Statistics, Central South University, Changsha, Hunan, China*

**Abstract**

The meshless methods combined with infinite element to deal with unbounded problems are developed in this paper. The meshless methods with moving least square algorithm, radial basis function interpolation and finite block method (Lagrange polynomial) are observed. With mapping of physical domain into a normalised square domain, the first order partial differential matrices both for regular and infinite elements (blocks) are determined. The governing equations and boundary conditions are formulated with the partial differential matrices. Numerical examples in the elasticity solid mechanics with non-homogenous and unbounded media are given to demonstrate the efficiency and accuracy of the meshless method combined with infinite elements. It is observed that the accurate numerical solutions of unbounded media can be obtained using the infinite elements at a much lesser computational effort than the conventional meshless methods in which unbounded media are represented by large number of collocation points.

*Key words*: meshless method, infinite element, mapping technique, differential matrix, functionally graded material.

*Corresponding: Email: p.h.wen@qmul.ac.uk; Tel: 0044 2078825371

## 1. Introduction

In the modeling of geomechanics problems involving soil-structure interaction, the soil medium is sometimes represented as a region of either infinite or semi-infinite extent. When considering such problems using finite element techniques, the traditional approach is to achieve the effect of unboundedness by incorporating a large number of elements. However, the use of such large finite element discretizations may result in an in ordinate amount of computational effort. Moreover, the truncated boundary may lead to erroneous results. In analytical study, several problems of solid mechanics involving unbounded domains have been solved in closed-form, which includes the elastic solutions for a point load applied in an infinite body, at the boundary of a half-space and at the interior of a semi-infinite solid etc. These solutions are called fundamental solutions in the boundary integral equation method or boundary element method (BEM) named in 1970s. BEM can be coupled with the FEM to give the appropriate boundary condition at the truncated boundary (see Zienkiewicz et al. [1]; Brebbia and Walker, [2]). However, it is often difficult to find the fundamental solutions, especially for nonlinear problems and for non-homogenous materials in advanced material science. .

The unbounded problems can be overcome by introducing mapped infinite elements, i.e. utilizing the infinite element to extend the FEM to unbounded domain problems (see Wood [3], Bettess and Zienkiewicz [4], Khalili et al [5], Zienkiewicz et al [6], Selvadurai and Karpurapu [7], Bettess [8]). The shape function describes the far-field characteristic of the problem, which can be obtained by using a mapping to transform the global infinite region into a local finite domain by Bettess [9], Damjanic and Owen [10], Zienkiewicz et al. [11], Simoni and Schrefier [12]. The comprehensive reviews for infinite element and its applications are given by Dong and Selvadurai [13] and Marques [14]

The appearance of the mesh free idea dates back to 1977 with the development of the Lagrangian method based on the kernel estimates method to model astrophysics problems by Monaghan and Gingold [15] and Lucy [16]. This method, named Smoothed Particle Hydrodynamics (SPH), is a particle method based on the idea of replacing the fluid by a set of moving particles and transforming the governing partial differential equations into the kernel estimates integrals [17]. There are many meshless approaches in the numerical engineering including the Diffuse Element Method (DEM), Element-Free Galerkin (EFG), Finite Point

Method, Meshless Local Petrov-Galerkin (MLPG) and Point Interpolation Method (PIM) etc. Meshless approximations have received much interest since Nayroles et al [18] proposed the diffuse element method [19,20]. Recently, Atluri and his colleagues presented a family of Meshless methods based on the Local weak Petrov-Galerkin formulation (MLPGs) for arbitrary partial differential equations [21,22,23,24,25] with Moving Least Square (MLS) approximation. Local Boundary Integral Equation method (LBIE) has been developed by Sladek et al [26,27,28] for the boundary value problems in anisotropic non-homogeneous media. The development of the Radial Basis Functions (RBF) as a truly meshless method has drawn attention (see Golberg et al [29]). Hardy [30] and Hon et al [31] developed the multiquadric interpolation method for solving linear partial differential equation. Recently, strong-form meshless methods also have been made progress, such as the Meshless Intervention Point (MIP) method, see Yang et al [32, 33, 34], and estimation of the qualitative convergence by Deng et al [35,36]). Based on the point collocation concept, the Finite Block Method (FBM) with mapping technique was proposed by Wen et al [37] and Li et al [38,39,40] to solve the heat transfer and elastodynamic 2D and 3D problems in the functionally graded media with excellent accuracy and convergence both in the Cartesian coordinate and polar coordinate systems.

In this paper, the meshless method of the point collocation type in strong form combined with infinite element to deal with unbounded media problems is developed first time. For the sake of convenience of analysis, the meshless collocation method with MLS approach, RBF interpolation and FBM are observed and tested. Firstly, the physical domain is mapped into a normalised square domain in which the nodes are uniformly/irregular distributed. Next, the first order of partial differential matrices for each element (block) are determined to present the governing equations in matrix form in terms of nodal values. Two dimensional non-homogenous problems are formulated both in Cartesian coordinate and polar coordinate systems respectively with infinite element. To observe the accuracy and efficiency using meshless methods combined with infinite elements, three numerical examples in elasticity solid mechanics are given and the comparisons are made with analytical solutions and numerical solutions by finite element method (ABAQUS) especially for the Functionally Graded Materials (FGM). It is clear that the meshless approach combined with infinite elements is an effective and accurate algorithm for unbounded problems in engineering.

## 2. The approximation schemes

*2.1 Moving lease-square scheme*

Consider a square mapped domain $\Omega$ shown in Figure 1(a) and interpolate the distribution of function $u$ in the sub-domain $\Omega_y$ centred at $\xi=(\xi,\eta)$ over a number of randomly distributed nodes $\xi_i=(\xi_i,\eta_i)$, $i=1,2,...,n_s$. The approximation of function $u$ at the point $\xi$ can be expressed by

$$u(\xi)=\mathbf{p}(\xi)^T\mathbf{a}(\xi), \tag{1}$$

where $\mathbf{a}(\xi)^T=\{a_1(\xi),a_2(\xi),...,a_m(\xi)\}$ is a vector of coefficients and $\mathbf{p}(\xi)^T=\{p_1(\xi),p_2(\xi),...,p_m(\xi)\}$ is a complete monomial basis, $m$ denotes the number of terms in the basis, i.e. for two dimensional problems. For example, $\mathbf{p}(\xi)^T=\{1,\xi,\eta\}$ when $m=3$ and $\mathbf{p}(\xi)^T=\{1,\xi,\eta,\xi^2,\xi\eta,\eta^2\}$ when $m=6$. The coefficient vector $\mathbf{a}(\xi)$ is to be determined by minimizing $L_2$ norm with a weighted function $\mathbf{w}(\xi,\eta)$ as following

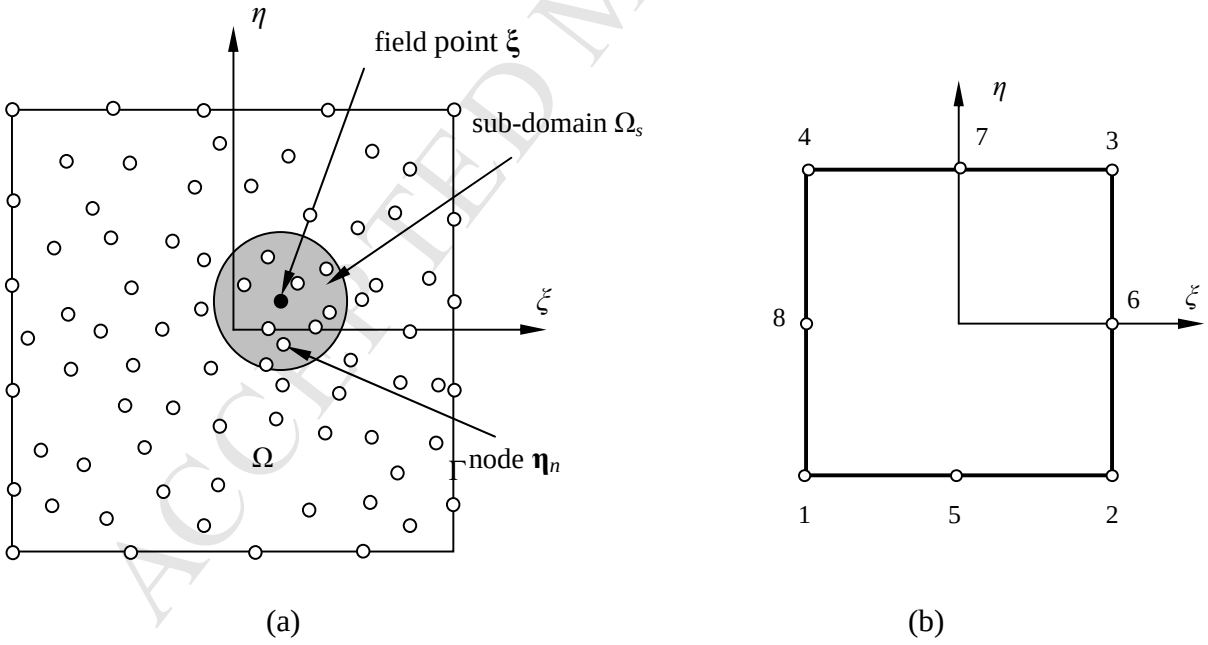


(a) (b)

Figure 1. Two-dimensional node distribution: (a) distribution of node and local support domain in mapped domain; (b) mapped domain with 8 seeds.

$$J(\mathbf{a}) = \sum_{i=1}^{n_s} w_i(\xi, \boldsymbol{\eta}_i)[\mathbf{p}^T(\boldsymbol{\eta}_i)\mathbf{a}(\xi) - \hat{u}_i(\boldsymbol{\eta}_i)]^2, \tag{2}$$

where $\boldsymbol{\eta}_i$ denotes the position vector of node $i$ in the support domain, $w_i(\xi, \boldsymbol{\eta})$ the weight function associated with the node $i$ with $w_i(\xi, \boldsymbol{\eta}) > 0$ for all $\boldsymbol{\eta}$ in the support domain and $\hat{u}_i$ is the fictitious nodal values, but in general not the values of the unknown trial function at the nodes, $\overline{u}_i(\boldsymbol{\eta})$. The stationary condition of $J$ in (2) with respect to $a_i$ $\partial J / \partial a_i = 0$ leads to the following equations in matrix form

$$\mathbf{A}(\xi)\mathbf{a}(\xi) - \mathbf{B}(\xi)\hat{\mathbf{u}} = 0, \tag{3}$$

where matrices $\mathbf{A}(\xi)$ and $\mathbf{B}(\xi)$ are defined

$$\mathbf{A}(\xi) = \mathbf{p}^T\mathbf{w}\mathbf{p}, \ \mathbf{B}(\xi) = \mathbf{p}^T\mathbf{w}. \tag{4}$$

The MLS approximation is well defined only when the matrix **A** in (3) is non-singular. Substituting (3) into (1) leads to the following relation

$$u(\xi) = \Phi^T(\xi)\hat{\mathbf{u}} = \sum_{k=1}^{n_s} \phi_k(\xi)\hat{u}_k, \tag{5}$$

where

$$\Phi^T(\xi) = \mathbf{p}^T(\xi)\mathbf{A}^{-1}(\xi)\mathbf{B}(\xi) \ \text{ or } \ \phi_k(\xi) = \sum_{j=1}^{m} p_j(\xi)[\mathbf{A}^{-1}(\xi)\mathbf{B}(\xi)]_{jk}.$$

Usually $\phi_k(\xi)$ is call the shape function of the MLS approximation corresponding to the nodal point $\boldsymbol{\eta}_k$. The support area of the nodal point $\boldsymbol{\eta}_k$ is taken to be a circle of radius $d_s$ centred at $\boldsymbol{\eta}_k$ (same size of local sub-domain centred at field point $\xi$). The selection of the radius $d_s$ is important in the MLS approximation because it determines the range of the interaction between the degrees of freedom defined at the considered nodes. The size of the support domain ($R$) should be sufficiently large to cover the nodes in the domain of definition hence ensuring the regularity of the matrix **A**. In the numerical process, the radius $d_s$ of the support domain will be determined by the minimum number of $n_s$ in the sub-domain. A fourth order spline type weight function is defined as

$$w_i(\xi, \boldsymbol{\eta}_i) = \begin{cases} 1 - 6\left(\dfrac{r}{d_s}\right)^2 + 8\left(\dfrac{r}{d_s}\right)^3 - 3\left(\dfrac{r}{d_s}\right)^4, & 0 \le r \le d_s, \\ 0, & d_s \le r, \end{cases} \tag{6}$$

where $r = |\boldsymbol{\xi} - \boldsymbol{\eta}_i|$. As the matrices in the shape function $\mathbf{A}^{-1}(\boldsymbol{\xi})$ and $\mathbf{B}(\boldsymbol{\xi})$ in (5) are functions of field point and nodal position in the support domain, the determination of high order derivatives of shape function with respect to the field point $\boldsymbol{\xi}$ will become more complicated in the numerical process. The partial derivatives of shape function can be obtained from Eq. (3) by straight forward differentiation, using MLS, as

$$\frac{\partial u}{\partial \xi} = \frac{\partial \Phi}{\partial \xi}\hat{\mathbf{u}} = \sum_{i=1}^{n_s} \frac{\partial \phi_i}{\partial \xi}\hat{u}_i\,, \qquad \frac{\partial u}{\partial \eta} = \frac{\partial \Phi}{\partial \eta}\hat{\mathbf{u}} = \sum_{i=1}^{n_s} \frac{\partial \phi_i}{\partial \eta}\hat{u}_i\,, \tag{7}$$

in which

$$\frac{\partial \phi_i}{\partial \xi} = \sum_{i=1}^{n_s}\left[\frac{\partial p_i}{\partial \xi}(\mathbf{A}^{-1}\mathbf{B}) + p_i\left(\frac{\partial \mathbf{A}^{-1}}{\partial \xi}\mathbf{B} + \mathbf{A}^{-1}\frac{\partial \mathbf{B}}{\partial \xi}\right)\right] .$$

$$\frac{\partial \phi_i}{\partial \eta} = \sum_{i=1}^{n_s}\left[\frac{\partial p_i}{\partial \eta}(\mathbf{A}^{-1}\mathbf{B}) + p_i\left(\frac{\partial \mathbf{A}^{-1}}{\partial \eta}\mathbf{B} + \mathbf{A}^{-1}\frac{\partial \mathbf{B}}{\partial \eta}\right)\right]. \tag{8}$$

As $\mathbf{A}^{-1}\mathbf{A} = \mathbf{I}$, the derivative of the inverse of matrix $\mathbf{A}$ with respect to $\boldsymbol{\xi}$ is given by

$$\frac{\partial \mathbf{A}^{-1}}{\partial \xi} = -\mathbf{A}^{-1}\frac{\partial \mathbf{A}}{\partial \xi}\mathbf{A}^{-1}, \quad \frac{\partial \mathbf{A}^{-1}}{\partial \eta} = -\mathbf{A}^{-1}\frac{\partial \mathbf{A}}{\partial \eta}\mathbf{A}^{-1}. \tag{9}$$

*2.2 Compact support radial basis function scheme*

Similar to MLS, the distribution of function *u* in the sub-domain $\Omega_y$ over a number of randomly distributed notes $\{\boldsymbol{\eta}_i\}$, $i = 1,2,...,n_s$ can be interpolated, at the point $\boldsymbol{\xi}$, by

$$u(\boldsymbol{\xi}) = \sum_{k=1}^{n_s} R_k(\boldsymbol{\xi})a_k + \sum_{j=1}^{m} p_j(\boldsymbol{\xi})b_j = \mathbf{R}(\boldsymbol{\xi} - \boldsymbol{\eta})\mathbf{a} + \mathbf{p}(\boldsymbol{\xi})\mathbf{b}\,, \tag{10}$$

where $\mathbf{R}(\boldsymbol{\xi} - \boldsymbol{\eta}) = \{R_1(\boldsymbol{\xi} - \boldsymbol{\eta}_1), R_2(\boldsymbol{\xi} - \boldsymbol{\eta}_2),..., R_{n_s}(\boldsymbol{\xi} - \boldsymbol{\eta}_{n_s})\}$ and $\mathbf{p}(\boldsymbol{\xi})$ are a set of radial basis functions centred around the point $\boldsymbol{\xi}$ and a set d-variate polynomials of degree *m* defined in (1), **a** and **b** are the unknown coefficients to be determined. The radial basis function is selected as multiquadrics [30] as

$$R_k(\boldsymbol{\xi} - \boldsymbol{\eta}_k) = \sqrt{c^2 + |\boldsymbol{\xi} - \boldsymbol{\eta}_k|^2}\,, \tag{11}$$

along with the constraints

$$\sum_{j=1}^{n_s} p_k(\boldsymbol{\eta}_j)a_j = 0, \quad 1 \le k \le m\,. \tag{12}$$

Then, a set of linear algebraic equations to determine coefficients **a** and **b** can be written, in the matrix form, as

$$\mathbf{R}_0\mathbf{a}+\mathbf{p}_0\mathbf{b}=\mathbf{u} \text{ and } \mathbf{p}_0^T\mathbf{a}=\mathbf{0}, \tag{13}$$

in which

$$\mathbf{R}_0=\begin{bmatrix} c & R_2(\boldsymbol{\eta}_1-\boldsymbol{\eta}_2) & \cdots & R_{n_s}(\boldsymbol{\eta}_1-\boldsymbol{\eta}_{n_s}) \\ R_1(\boldsymbol{\eta}_2-\boldsymbol{\eta}_1) & c & \cdots & R_{n_s}(\boldsymbol{\eta}_2-\boldsymbol{\eta}_{n_s}) \\ \cdot & \cdot & \cdots & \cdot \\ \cdot & \cdot & \cdots & \cdot \\ \cdot & \cdot & \cdots & \cdot \\ R_1(\boldsymbol{\eta}_{n_s}-\boldsymbol{\eta}_1) & R_2(\boldsymbol{\eta}_{n_s}-\boldsymbol{\eta}_2) & \cdots & c \end{bmatrix} \tag{14}$$

and

$$\mathbf{p}_0=\begin{bmatrix} p_1(\boldsymbol{\eta}_1) & p_2(\boldsymbol{\eta}_1) & \cdots & p_m(\boldsymbol{\eta}_1) \\ p_1(\boldsymbol{\eta}_2) & p_2(\boldsymbol{\eta}_2) & \cdots & p_m(\boldsymbol{\eta}_2) \\ \cdot & \cdot & \cdots & \cdot \\ \cdot & \cdot & \cdots & \cdot \\ \cdot & \cdot & \cdots & \cdot \\ p_1(\boldsymbol{\eta}_{n_s}) & p_2(\boldsymbol{\eta}_{n_s}) & \cdots & p_m(\boldsymbol{\eta}_{n_s}) \end{bmatrix}. \tag{15}$$

Obviously matrix $\mathbf{R}_0$ is symmetric and well defined. Solving equations (13) gives

$$\mathbf{a}=\mathbf{R}_0^{-1}\left[\mathbf{I}-\mathbf{p}_0\left(\mathbf{p}_0^T\mathbf{R}_0^{-1}\mathbf{p}_0\right)^{-1}\mathbf{p}_0^T\mathbf{R}_0^{-1}\right]\mathbf{u}=\mathbf{G}\,\mathbf{u},\ \mathbf{b}=\left(\mathbf{p}_0^T\mathbf{R}_0^{-1}\mathbf{p}_0\right)^{-1}\mathbf{p}_0^T\mathbf{R}_0^{-1}\mathbf{u}=\mathbf{H}\mathbf{u}, \tag{16}$$

where **I** denotes the diagonal unit matrix. Substituting the coefficients **a** and **b** in (16) into (10), we can obtain the shape function in (10) same as MLS method as

$$\begin{aligned} &\mathbf{u}(\boldsymbol{\xi})=\sum_k^{n_s}\phi_k(\boldsymbol{\xi})u_k, \\ &\phi_k(\boldsymbol{\xi})=\sum_{i=1}^{n_s}R_i(\boldsymbol{\xi})G_{ik}+\sum_{j=1}^{m}p_j(\boldsymbol{\xi})H_{jk}. \end{aligned} \tag{17}$$

It is worth noting that the shape function depends uniquely on the distribution of scattered nodes within the support domain and has the Kronecker Delta property. As the inverse matrix of coefficient $\mathbf{R}_0^{-1}$ is function of distributed node $\boldsymbol{\eta}$ only in the support domain, it is much simpler to evaluate the partial derivatives of shape function by

$$\frac{\partial \phi_k}{\partial \xi} = \sum_{i=1}^{n_s} \frac{\partial R_i(\xi)}{\partial \xi} G_{ik} + \sum_{j=1}^{m} \frac{\partial p_j(\xi)}{\partial \xi} H_{jk},$$
$$\frac{\partial \phi_k}{\partial \eta} = \sum_{i=1}^{n_s} \frac{\partial R_i(\xi)}{\partial \eta} G_{ik} + \sum_{j=1}^{m} \frac{\partial p_j(\xi)}{\partial \eta} H_{jk}. \tag{18}$$

*. 2.3 Finite block method (Lagrange polynomials)*

Consider a set of nodes uniformly distributed in the normalised domain in Figure 2 with numbering system of node collocation at $\xi_k$, $k=(j-1)\times N_\xi + i$, $i=1,2,...,N_\xi$ and $j=1,2,...,N_\eta$, where $N_\alpha$ are numbers of nodes along two axes. By two dimension Lagrange interpolation polynomials, the function $u(\xi)$ can be approximated by

$$u(\xi) = \sum_{i=1}^{N_1}\sum_{j=1}^{N_2} F(\xi,\xi_i)G(\eta,\eta_j)u^{(k)}, \tag{19}$$

where

$$F(\xi,\xi_i) = \prod_{\substack{m=1 \\ m\neq i}}^{N_1} \frac{(\xi-\xi_m)}{(\xi_i-\xi_m)},\ G(\eta,\eta_j) = \prod_{\substack{n=1 \\ n\neq j}}^{N_2} \frac{(\eta-\eta_n)}{(\eta_j-\eta_n)}. \tag{20}$$

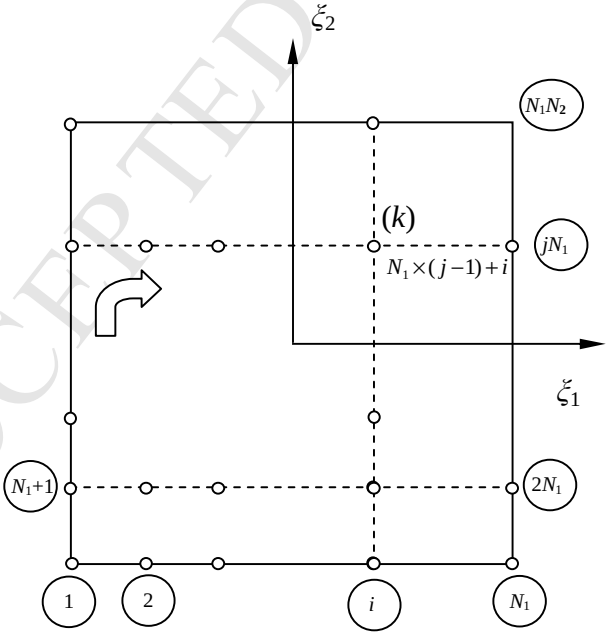


Figure 2. Uniformly distributed nodes in mapped domain and numbering system for FBM.

Therefore, the shape functions can be constructed as

$$\phi_k = F(\xi,\xi_i)G(\eta,\eta_j) = \prod_{\substack{m=1\\ m\neq i}}^{N_\xi} \frac{(\xi-\xi_m)}{(\xi_i-\xi_m)} \prod_{\substack{n=1\\ n\neq j}}^{N_\eta} \frac{(\eta-\eta_n)}{(\eta_j-\eta_n)}. \tag{21}$$

Then the number of nodes in total is $M = N_\xi \times N_\eta$. Thereafter, the first order partial differential of shape function can be determined easily with respects to $\xi$

$$\frac{\partial \phi_k}{\partial \xi} = \frac{\partial F(\xi,\xi_i)}{\partial \xi} G(\eta,\eta_j), \quad \frac{\partial \phi_k}{\partial \eta} = F(\xi,\xi_i)\frac{\partial G(\eta,\eta_j)}{\partial \eta}, \tag{22}$$

where

$$\frac{\partial F}{\partial \xi} = \sum_{l=1}^{N_\xi} \prod_{i=1, i\neq i, i\neq l}^{N_\xi} (\xi-\xi_i) \Big/ \prod_{m=1, m\neq i}^{N_\xi} (\xi_i-\xi_m) \tag{23}$$

and

$$\frac{\partial G}{\partial \eta} = \sum_{l=1}^{N_\eta} \prod_{j=1, j\neq i, j\neq l}^{N_\eta} (\eta-\eta_j) \Big/ \prod_{n=1, n\neq j}^{N_\eta} (\eta_j-\eta_n). \tag{24}$$

For Lagrange interpolation, the shape function in (20) depends uniquely on the distribution of scattered nodes within the support domain and has the Kronecker Delta property same as RBF approach.

*2.4 Partial differential matrix*

For different approaches, the first order partial differentials at each node introduced above can be evaluated, in the form of vector, as

$$\mathbf{u}_{,\alpha} = \mathbf{U}_\alpha = \mathbf{D}_\alpha \mathbf{u}, \ \mathbf{D}_\alpha = \{\phi_{lk}\}_{M\times M}, \ (k,l = 1,2,...,M), \tag{25a}$$

in which $\alpha = \xi, \eta$, $\mathbf{D}_\alpha$ is the first order differential matrix determined by each shape functions,

$$\mathbf{u}_{,\alpha} = \left\{ \frac{\partial u(\xi^{(1)},\eta^{(1)})}{\partial \alpha}, \frac{\partial u(\xi^{(2)},\eta^{(2)})}{\partial \alpha}, ..., \frac{\partial u(\xi^{(M)},\eta^{(M)})}{\partial \alpha} \right\}^{\mathrm{T}}, \quad \mathbf{u} = \{u^{(1)}, u^{(2)}, ..., u^{(M)}\}^{\mathrm{T}}. \tag{25b}$$

For the moving least square method, vector $\mathbf{u}$ should be changed to fictitious displacement $\hat{\mathbf{u}}$. Furthermore, the $L$-th order partial differentials in two dimensional problems with respect to both coordinates $\xi$ and $\eta$ can be obtained approximately by

$$u^{(mn)}_{,\xi\eta}(\xi,\eta) = \frac{\partial^{m+n} u}{\partial \xi^m \partial \eta^n}, \quad m+n = L. \tag{26}$$

Therefore, the vectors of the higher order partial differentials can be constructed, in terms of the first order partial differential matrices $\mathbf{D}_\xi$ and $\mathbf{D}_\eta$, as

$$\mathbf{u}_{,\xi\eta}^{(mn)} \approx \mathbf{D}_\xi^m \mathbf{D}_\eta^n \mathbf{u}. \tag{27}$$

## 3. Coordinate transform and mapping differential matrix

*3.1. Two dimensional problem*

For two dimensional problems, any quadratic block with 8 seeds shown in Figure 4(a) can be mapped into a square domain (normalised) using following shape functions

$$\begin{aligned} N_i &= \frac{1}{4}(1+\bar{\xi}_i\xi)(1+\bar{\eta}_i\eta)(\bar{\xi}_i\xi+\bar{\eta}_i\eta-1) \quad \text{for} \quad i=1,2,3,4, \\ N_i &= \frac{1}{2}(1-\xi^2)(1+\bar{\eta}_i\eta) \quad \text{for} \quad i=5,7, \\ N_i &= \frac{1}{2}(1-\eta^2)(1+\bar{\xi}_i\xi) \quad \text{for} \quad i=6,8, \end{aligned} \tag{28}$$

where $(\bar{\xi}_i,\bar{\eta}_i)$ $i=1,2,...,8$ are the seed coordinates shown in Figure 1(b). The coordinate transform (mapping) can be written as

$$x=\sum_{k=1}^{8} N_k(\xi,\eta)x_k, \;\; y=\sum_{k=1}^{8} N_k(\xi,\eta)y_k \;. \tag{29}$$

For partial differentials of function $u(x,y)$ in Cartesian coordinate system, one has

$$\frac{\partial u}{\partial x}=\frac{1}{J}\left(\beta_{11}\frac{\partial u}{\partial \xi}+\beta_{12}\frac{\partial u}{\partial \eta}\right), \;\; \frac{\partial u}{\partial y}=\frac{1}{J}\left(\beta_{21}\frac{\partial u}{\partial \xi}+\beta_{22}\frac{\partial u}{\partial \eta}\right), \tag{30}$$

where

$$J=\begin{vmatrix} \dfrac{\partial x}{\partial \xi} & \dfrac{\partial x}{\partial \eta} \\ \dfrac{\partial y}{\partial \xi} & \dfrac{\partial y}{\partial \eta} \end{vmatrix}, \;\; \beta_{11}=\frac{\partial y}{\partial \eta}, \beta_{12}=-\frac{\partial y}{\partial \xi}, \beta_{21}=-\frac{\partial x}{\partial \eta}, \beta_{22}=\frac{\partial x}{\partial \xi}. \tag{31}$$

Thus, the first partial differential matrices can be written, in physical domain, as

$$\mathbf{U}_x=\mathbf{\Delta}_{11}\mathbf{U}_\xi+\mathbf{\Delta}_{12}\mathbf{U}_\eta=\left(\mathbf{\Delta}_{11}\mathbf{D}_\xi+\mathbf{\Delta}_{12}\mathbf{D}_\eta\right)\mathbf{u}=\mathbf{D}_x\mathbf{u}, \tag{32}$$

$$\mathbf{U}_y=\mathbf{\Delta}_{21}\mathbf{U}_\xi+\mathbf{\Delta}_{22}\mathbf{U}_\eta=\left(\mathbf{\Delta}_{21}\mathbf{D}_\xi+\mathbf{\Delta}_{22}\mathbf{D}_\eta\right)\mathbf{u}=\mathbf{D}_y\mathbf{u}, \tag{33}$$

in which

$$\mathbf{\Lambda}_{ij}=\begin{pmatrix}\beta_{ij}^{(1)}/J^{(1)} & 0 & ... & 0\\ 0 & \beta_{ij}^{(2)}/J^{(2)} & ... & 0\\ ... & ... & ... & ...\\ 0 & 0 & ... & \beta_{ij}^{(M)}/J^{(M)}\end{pmatrix}, \tag{34}$$

$\beta_{ij}^{(k)}/J^{(k)}$ is calculated from (31) at collocation point $\boldsymbol{\xi}_k=(\xi_k,\eta_k)$ and differential matrices in the normalized domain $\mathbf{D}_\xi$ and $\mathbf{D}_\eta$ are given in (24). It means that the first partial differentials in the practical Cartesian coordinate can be obtained in terms of the first order partial differential matrix in the mapped domain, where $|\xi|\le 1;|\eta|\le 1$, and nodal values.

*3.2 Three dimensional problem*

For three dimension problem, quadratic shape function with 20 seeds is used. Shape functions can be written as follows [40]

$$\begin{aligned}
&N_i=\frac{1}{8}(1+\bar{\xi}_i\xi)(1+\bar{\eta}_i\eta)(1+\bar{\varsigma}_i\varsigma)(\bar{\xi}_i\xi+\bar{\eta}_i\eta+\bar{\varsigma}_i\varsigma-2)\ \text{for}\ i=1,2,3,4,5,6,7,8,\\
&N_i=\frac{1}{4}(1-\xi^2)(1+\bar{\eta}_i\eta)(1+\bar{\varsigma}_i\varsigma)\ \ \text{for}\ i=9,11,17,19,\\
&N_i=\frac{1}{4}(1-\eta^2)(1+\bar{\varsigma}_i\varsigma)(1+\bar{\xi}_i\xi)\ \ \text{for}\ i=10,12,18,20,\\
&N_i=\frac{1}{4}(1-\varsigma^2)(1+\bar{\xi}_i\xi)(1+\bar{\eta}_i\eta)\ \ \text{for}\ i=13,14,15,16.
\end{aligned} \tag{35}$$

Same as two dimension and the coordinate transform (mapping) can be written as

$$x=\sum_{k=1}^{20}N_k(\xi,\eta,\varsigma)x_k,\ \ y=\sum_{k=1}^{20}N_k(\xi,\eta,\varsigma)y_k,\ \ z=\sum_{k=1}^{20}N_k(\xi,\eta,\varsigma)z_k\ . \tag{36}$$

Then the partial differentials of shape functions are

$$\begin{aligned}
\frac{\partial u}{\partial x}&=\frac{1}{J}\left(\frac{\partial u}{\partial\xi}\beta_{11}+\frac{\partial u}{\partial\eta}\beta_{12}+\frac{\partial u}{\partial\varsigma}\beta_{13}\right),\\
\frac{\partial u}{\partial y}&=\frac{1}{J}\left(\frac{\partial u}{\partial\xi}\beta_{21}+\frac{\partial u}{\partial\eta}\beta_{22}+\frac{\partial u}{\partial\varsigma}\beta_{23}\right),\\
\frac{\partial u}{\partial z}&=\frac{1}{J}\left(\frac{\partial u}{\partial\xi}\beta_{31}+\frac{\partial u}{\partial\eta}\beta_{32}+\frac{\partial u}{\partial\varsigma}\beta_{33}\right),
\end{aligned} \tag{37}$$

where

$$J=\begin{vmatrix} \dfrac{\partial x}{\partial \xi} & \dfrac{\partial x}{\partial \eta} & \dfrac{\partial x}{\partial \varsigma} \\ \dfrac{\partial y}{\partial \xi} & \dfrac{\partial y}{\partial \eta} & \dfrac{\partial y}{\partial \varsigma} \\ \dfrac{\partial z}{\partial \xi} & \dfrac{\partial z}{\partial \eta} & \dfrac{\partial z}{\partial \varsigma} \end{vmatrix} \tag{38}$$

and coefficients

$$\begin{aligned} &\beta_{11}=\frac{\partial y}{\partial \eta}\frac{\partial z}{\partial \varsigma}-\frac{\partial y}{\partial \varsigma}\frac{\partial z}{\partial \eta},\beta_{12}=-\frac{\partial y}{\partial \xi}\frac{\partial z}{\partial \varsigma}+\frac{\partial y}{\partial \varsigma}\frac{\partial z}{\partial \xi},\beta_{13}=\frac{\partial y}{\partial \xi}\frac{\partial z}{\partial \eta}-\frac{\partial y}{\partial \eta}\frac{\partial z}{\partial \xi}, \\ &\beta_{21}=-\frac{\partial x}{\partial \eta}\frac{\partial z}{\partial \varsigma}+\frac{\partial x}{\partial \varsigma}\frac{\partial z}{\partial \eta},\beta_{22}=\frac{\partial x}{\partial \xi}\frac{\partial z}{\partial \varsigma}-\frac{\partial x}{\partial \varsigma}\frac{\partial z}{\partial \xi},\beta_{23}=-\frac{\partial x}{\partial \xi}\frac{\partial z}{\partial \eta}+\frac{\partial x}{\partial \eta}\frac{\partial z}{\partial \xi}, \\ &\beta_{31}=\frac{\partial x}{\partial \eta}\frac{\partial y}{\partial \varsigma}-\frac{\partial x}{\partial \varsigma}\frac{\partial y}{\partial \eta},\beta_{32}=-\frac{\partial x}{\partial \xi}\frac{\partial y}{\partial \varsigma}+\frac{\partial x}{\partial \varsigma}\frac{\partial y}{\partial \xi},\beta_{33}=\frac{\partial x}{\partial \xi}\frac{\partial y}{\partial \eta}-\frac{\partial x}{\partial \eta}\frac{\partial y}{\partial \xi}. \end{aligned} \tag{39}$$

Therefore, the first order nodal partial differential matrices in Cartesian coordinate system can be written, in matrix form, as

$$\begin{aligned} &\mathbf{U}_x=\boldsymbol{\Delta}_{11}\mathbf{U}_\xi+\boldsymbol{\Delta}_{12}\mathbf{U}_\eta+\boldsymbol{\Delta}_{13}\mathbf{U}_\varsigma=\left(\boldsymbol{\Delta}_{11}\mathbf{D}_\xi+\boldsymbol{\Delta}_{12}\mathbf{D}_\eta+\boldsymbol{\Delta}_{13}\mathbf{D}_\varsigma\right)\mathbf{u}=\mathbf{D}_x\mathbf{u}, \\ &\mathbf{U}_y=\boldsymbol{\Delta}_{21}\mathbf{U}_\xi+\boldsymbol{\Delta}_{22}\mathbf{U}_\eta+\boldsymbol{\Delta}_{23}\mathbf{U}_\varsigma=\left(\boldsymbol{\Delta}_{21}\mathbf{D}_\xi+\boldsymbol{\Delta}_{22}\mathbf{D}_\eta+\boldsymbol{\Delta}_{23}\mathbf{D}_\varsigma\right)\mathbf{u}=\mathbf{D}_y\mathbf{u}, \\ &\mathbf{U}_z=\boldsymbol{\Delta}_{31}\mathbf{U}_\xi^{)}+\boldsymbol{\Delta}_{32}\mathbf{U}_\eta+\boldsymbol{\Delta}_{33}\mathbf{U}_\varsigma=\left(\boldsymbol{\Delta}_{31}\mathbf{D}_\xi+\boldsymbol{\Delta}_{32}\mathbf{D}_\eta+\boldsymbol{\Delta}_{33}\mathbf{D}_\varsigma\right)\mathbf{u}=\mathbf{D}_z\mathbf{u}, \end{aligned} \tag{40}$$

where $\boldsymbol{\Delta}_{ij}$ is defined in (34), matrix, $\mathbf{D}_\xi$, $\mathbf{D}_\eta$ and $\mathbf{D}_\varsigma$ are first order of partial differential matrices defined in (24). Again, the first partial differentials can be determined in terms of the first order differential matrix in mapped domain, $|\xi|\le 1;|\eta|\le 1;|\varsigma|\le 1$, with nodal values in the equation above. In addition, the higher order partial differentials with respect to Cartesian coordinates $(xyz)$ can be written as

$$U_{xyz}^{(mnl)}(x,y,z)=\frac{\partial^{m+n+l}u}{\partial x^m\partial y^n\partial z^l} \tag{41}$$

and the nodal values of the above partial differential are obtained in the matrix form by

$$\mathbf{U}_{xyz}^{(mnl)}=\mathbf{D}_x^m\mathbf{D}_y^n\mathbf{D}_z^l\mathbf{u}. \tag{42}$$

## 4. Two dimensional infinite elements

This element type was introduced by Zienkiewicz [1] and will be used in the meshless approach. Mapped infinite elements use a simple mapping technique akin to the isoparameteric formulation [14] but employing two set of element trial functions: (1) Geometry description is performed by means of specially devised mapping function; (2) Locations of collocation point are determined in real physical domain; (3) Partial differential matrices are obtained in the real domain. For two-dimensional problems, two simplest infinite elements are utilised in this paper:

(1) Four-seeds mapping

In the normalised domain, the edge of right hand side $(\xi = 1)$ is mapped to infinite place as shown in Figure 3. The mapping functions are

$$N_1 = -\frac{\xi(1-\eta)}{(1-\xi)},\ N_2 = \frac{(1+\xi)(1-\eta)}{2(1-\xi)},\ N_3 = \frac{(1+\xi)(1+\eta)}{2(1-\xi)},\ N_4 = -\frac{\xi(1+\eta)}{(1-\xi)} \tag{43}$$

and the mapped geometry

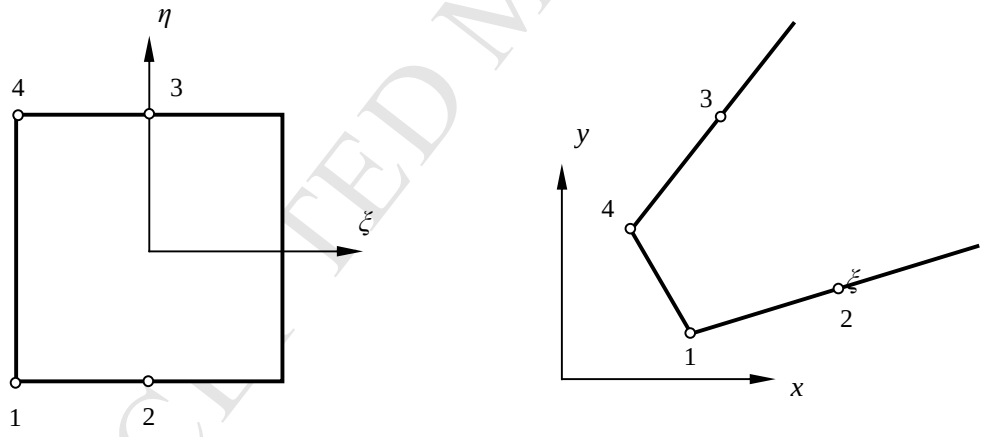


(a) (b)

Figure 3. Four nodes mapping: (a) normalized domain; (b) physical domain.

$$x = \sum_{i=1}^{4} N_i(\xi,\eta)x_i,\ y = \sum_{i=1}^{4} N_i(\xi,\eta)y_i\ . \tag{44}$$

Also the locations for each collocation point can be specified as

$$x_k = \sum_{i=1}^{4} N_i(\xi_k,\eta_k)x_i,\ y_k = \sum_{i=1}^{4} N_i(\xi_k,\eta_k)y_i\ . \tag{45}$$

Then their partial differentials respect to $\xi$ and $\eta$ are given

$$\frac{\partial N_1}{\partial \xi}=-\frac{(1-\eta)}{(1-\xi)^2},\ \frac{\partial N_2}{\partial \xi}=\frac{(1-\eta)}{(1-\xi)^2},\ \frac{\partial N_3}{\partial \xi}=\frac{(1+\eta)}{(1-\xi)^2},\ \frac{\partial N_4}{\partial \xi}=-\frac{(1+\eta)}{(1-\xi)^2} \tag{46}$$

and

$$\frac{\partial N_1}{\partial \eta}=\frac{\xi}{(1-\xi)},\ \frac{\partial N_2}{\partial \eta}=-\frac{(1+\xi)}{2(1-\xi)},\ \frac{\partial N_3}{\partial \eta}=\frac{(1+\xi)}{2(1-\xi)},\ \frac{\partial N_4}{\partial \eta}=-\frac{\xi}{(1-\xi)}. \tag{47}$$

It is clear that the first derivative matrices for all collocation points in (32) and (33) are still valid for the infinite element except the nodes at $\xi=1$.

(2) Five-seeds mapping

Same as four seed mapping, the edge of right hand side ($\xi=1$) is mapped to infinite place as shown in Figure 4. The mapping functions are given as

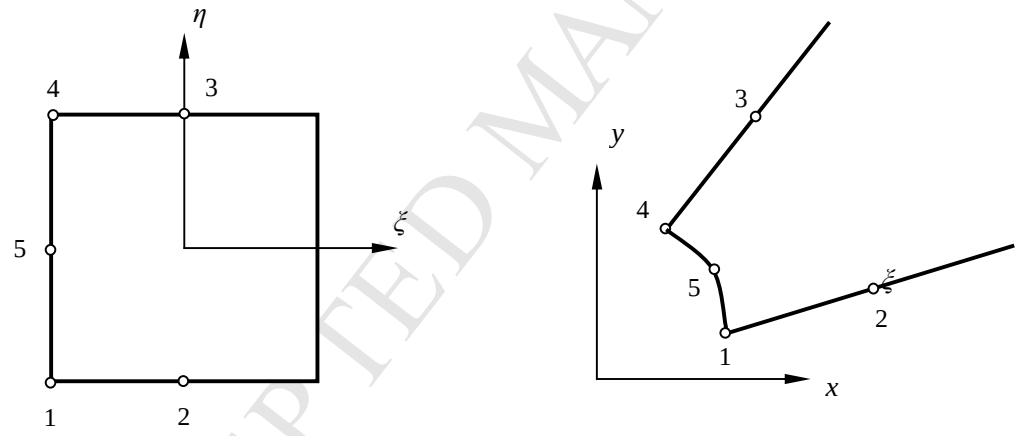


(a) (b)

Figure 4. Five nodes mapping: (a) normalized domain; (b) physical domain.

$$\begin{aligned} &N_1=-\frac{(1+\xi+\eta)(1-\eta)}{(1-\xi)},\ N_2=\frac{(1+\xi)(1-\eta)}{2(1-\xi)},\ N_3=\frac{(1+\xi)(1+\eta)}{2(1-\xi)},\\ &N_4=\frac{(-1+\eta-\xi)(1+\eta)}{(1-\xi)},\ N_5=\frac{2(1-\eta^2)}{(1-\xi)}. \end{aligned} \tag{48}$$

Same as four node mapping, the coordinate transformation is preformed as

$$x=\sum_{i=1}^{4}N_i(\xi,\eta)x_i,\ \ y=\sum_{i=1}^{5}N_i(\xi,\eta)y_i\ , \tag{49}$$

and the locations for each collocation point can be specified as

$$x_k = \sum_{i=1}^{5} N_i(\xi_k, \eta_k) x_i,\ y_k = \sum_{i=1}^{5} N_i(\xi_k, \eta_k) y_i\,. \tag{50}$$

Then their partial differentials respect to $\xi$ and $\eta$ are given as

$$\begin{aligned} &\frac{\partial N_1}{\partial \xi} = -\frac{(1-\eta)(2+\eta)}{(1-\xi)^2},\ \frac{\partial N_2}{\partial \xi} = \frac{(1-\eta)}{(1-\xi)^2},\ \frac{\partial N_3}{\partial \xi} = \frac{(1+\eta)}{(1-\xi)^2}, \\ &\frac{\partial N_4}{\partial \xi} = -\frac{(1+\eta)(2-\eta)}{(1-\xi)^2},\ \frac{\partial N_5}{\partial \xi} = \frac{2(1-\eta^2)}{(1-\xi)^2}. \end{aligned} \tag{51}$$

and

$$\begin{aligned} &\frac{\partial N_1}{\partial \eta} = \frac{(2\eta+\xi)}{(1-\xi)},\ \frac{\partial N_2}{\partial \eta} = -\frac{(1+\xi)}{2(1-\xi)},\ \frac{\partial N_3}{\partial \eta} = \frac{(1+\xi)}{2(1-\xi)}, \\ &\frac{\partial N_4}{\partial \eta} = \frac{(2\eta-\xi)}{(1-\xi)},\ \frac{\partial N_5}{\partial \eta} = -\frac{4\eta}{(1-\xi)}. \end{aligned} \tag{52}$$

The physical values including displacements and stresses are zero at infinite. Two and three dimensional mapping and shape functions for different types of the infinite element used in the finite element method are catalogued in [14] by Marques. Zienkiewicz [6] presented an extensive survey of procedures used for finite element unbounded domain analysis, grouping them in accordance with the nature of the algorithm.

## 5. Meshless method for unbounded media

*5.1. Cartesian coordinate system,*

Assuming that the material properties are dependent on the spatial coordinates in a non-homogeneous material, the relationship between stress and strain isotropic materials, in the plane stress state and Cartesian coordinate system, gives

$$\sigma_x = Q_1 \frac{\partial u_x}{\partial x} + Q_2 \frac{\partial u_y}{\partial y},\ \sigma_y = Q_2 \frac{\partial u_x}{\partial x} + Q_1 \frac{\partial u_y}{\partial y},\ \tau_{xy} = Q_3 \left( \frac{\partial u_x}{\partial y} + \frac{\partial u_y}{\partial x} \right). \tag{53}$$

For plane stress elasticity, material mechanical coefficients are, for isotropic on-homogenous, given as

$$Q_1 = \frac{E(\mathbf{x})}{1-\nu^2(\mathbf{x})},\ Q_2 = \frac{\nu(\mathbf{x})E(\mathbf{x})}{1-\nu^2(\mathbf{x})},\ Q_3 = G(\mathbf{x})\,, \tag{54}$$

where $E,\nu$ are Young's modulus and Poisson's ratio, $G$ is shear modulus. The equilibrium equations give

$$\frac{\partial \sigma_x}{\partial x}+\frac{\partial \tau_{xy}}{\partial y}+b_x=0,\ \frac{\partial \tau_{xy}}{\partial x}+\frac{\partial \sigma_y}{\partial y}+b_y=0, \tag{55}$$

where $b_x$ and $b_y$ are body forces. Applying the differential matrices over (55) results, with considering (32)(33)(53)(54) in matrix form, as

$$\begin{aligned}&\left(\mathbf{D}_x\mathbf{Q}_1\mathbf{D}_x+\mathbf{D}_y\mathbf{Q}_3\mathbf{D}_y\right)\mathbf{u}_x+\left(\mathbf{D}_x\mathbf{Q}_2\mathbf{D}_y+\mathbf{D}_y\mathbf{Q}_3\mathbf{D}_x\right)\mathbf{u}_y+\mathbf{b}_x=\mathbf{0},\\&\left(\mathbf{D}_y\mathbf{Q}_2\mathbf{D}_x+\mathbf{D}_x\mathbf{Q}_3\mathbf{D}_y\right)\mathbf{u}_x+\left(\mathbf{D}_x\mathbf{Q}_3\mathbf{D}_x+\mathbf{D}_y\mathbf{Q}_1\mathbf{D}_y\right)\mathbf{u}_y+\mathbf{b}_y=\mathbf{0},\end{aligned} \tag{56}$$

where $\mathbf{u}_\beta$ and $\mathbf{b}_\beta$ $(\beta=x,y)$ are vectors of nodal displacement and body force vectors, and $\mathbf{Q}_l=\mathbf{diag}[Q_l^{(k)}]$ is diagonal matrices, in which $Q_l^{(k)}$ $(l=1,2,3)$ indicates the elasticity coefficient at node $k$. The boundary conditions give

$$\begin{aligned}&u_\beta(\mathbf{x})=u_\beta^0(\mathbf{x}), &&\mathbf{x}\in\Gamma_u\\&t_\beta(\mathbf{x})=t_\beta^0(\mathbf{x}), &&\mathbf{x}\in\Gamma_q\end{aligned} \tag{57}$$

where $u_\beta^0$ and $t_\beta^0$ are specified displacements and tractions on the boundary. Obviously there are $2M$ linear algebraic equations from (56) and (58), and therefore, all nodal values of displacement should be determined. Unlike the traditional meshless method, the physical domain is divided into few blocks by using the finite block method. In this case, the continuous condition on the smooth interface except two ends (joints) between blocks I and II gives

$$u_\beta^I(\mathbf{x})-u_\beta^{II}(\mathbf{x})=0,\ t_\beta^I(\mathbf{x})+t_\beta^{II}(\mathbf{x})=0. \qquad \mathbf{x}\in\Gamma_{\text{int}} \tag{58}$$

However, at corner joint, both the displacement continuity conditions and point equilibrium equations should be considered as

$$u_\beta^I(\mathbf{x})=u_\beta^{II}(\mathbf{x})=\ldots=u_\beta^X(\mathbf{x}), \tag{59}$$

$$\begin{aligned}&\sum_{q=I}^{X}\left(\sigma_x^{(q)}[\sin\theta_2^{(q)}-\sin\theta_1^{(q)}]-\tau_{xy}^{(q)}[\cos\theta_2^{(q)}-\cos\theta_1^{(q)}]\right)=0,\\&\sum_{q=I}^{X}\left(\tau_{xy}^{(q)}[\sin\theta_2^{(q)}-\sin\theta_1^{(q)}]-\sigma_y^{(q)}[\cos\theta_2^{(q)}-\cos\theta_1^{(q)}]\right)=0,\end{aligned} \tag{60}$$

where $\theta_2^{(q)}$ and $\theta_1^{(q)}$ are starting and ending angles at joint for block $q$ at the joint shown in Figure 5.

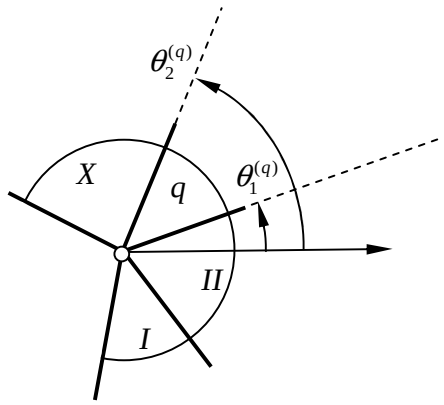


Figure 5. Joint with blocks: starting and ending angles for each block.

*5.2. Polar coordinate system*

In many cases, the polar coordinate system is much convenient with circular boundary. Consider the 2D elasticity of the domain $\Omega$ with boundary $\Gamma$ in functionally graded media in polar coordinate system. It is assumed that the materials are directionally dependent and all material coefficients could be dependent on the spatial coordinates in a non-homogeneous material. The equilibrium equations for two dimensional plane-stress are

$$\sigma_r = Q_1\varepsilon_r + Q_2\varepsilon_\theta,\ \sigma_\theta = Q_2\varepsilon_r + Q_1\varepsilon_\theta,\ \tau_{xy} = Q_3\gamma_{r\theta}, \tag{61}$$

in which all material coefficients vary with coordinates $r$ and $\theta$, and

$$\varepsilon_r = \frac{\partial u_r}{\partial r}, \varepsilon_\theta = \frac{1}{r}\frac{\partial u_\theta}{\partial \theta} + \frac{u_r}{r}, \gamma_{r\theta} = \frac{\partial u_\theta}{\partial r} + \frac{1}{r}\frac{\partial u_r}{\partial \theta} - \frac{u_\theta}{r} \tag{62}$$

are normal and shear strains respectively. For static problem in the polar coordinate, one has the equilibrium equations as the following

$$\begin{aligned} &\frac{\partial \sigma_r}{\partial r} + \frac{1}{r}\frac{\partial \tau_{r\theta}}{\partial \theta} + \frac{\sigma_r - \sigma_\theta}{r} = 0, \\ &\frac{\partial \tau_{r\theta}}{\partial r} + \frac{1}{r}\frac{\partial \sigma_\theta}{\partial \theta} + \frac{2\tau_{r\theta}}{r} = 0. \end{aligned} \tag{63}$$

For isotropic homogeneous functionally graded material and plane-stress problems, the coefficients

$$Q_1(r,\theta) = \frac{E(r,\theta)}{1-\nu^2(r,\theta)},\ Q_2(r,\theta) = \frac{\nu(r,\theta)E(r,\theta)}{1-\nu^2(r,\theta)},\ Q_3(r,\theta) = G(r,\theta)\ . \tag{64}$$

Applying the mapping technique and differential matrices, stresses can be obtained in matrix form in terms of the nodal values

$$\begin{aligned}
&\mathbf{S}_r = \mathbf{Q}_1\mathbf{D}_r\mathbf{u}_r + \mathbf{Q}_2\hat{\mathbf{R}}\left(\mathbf{D}_\theta\mathbf{u}_\theta + \mathbf{u}_r\right),\\
&\mathbf{S}_\theta = \mathbf{Q}_2\mathbf{D}_r\mathbf{u}_r + \mathbf{Q}_1\hat{\mathbf{R}}\left(\mathbf{D}_\theta\mathbf{u}_\theta + \mathbf{u}_r\right),\\
&\mathbf{S}_{r\theta} = \mathbf{Q}_3\left(\mathbf{D}_r\mathbf{u}_\theta + \hat{\mathbf{R}}\mathbf{D}_\theta\mathbf{u}_r - \hat{\mathbf{R}}\mathbf{u}_\theta\right).
\end{aligned} \tag{65}$$

where $\mathbf{D}_r$ and $\mathbf{D}_\theta$ are first order partial differential matrices obtained in the same way in Cartesian coordinate system, $\hat{\mathbf{R}} = \mathbf{diag}[1/r_k]$ is diagonal matrices. Substituting (61) into the equilibrium equations (63) gives the system equations as

$$\begin{aligned}
&\mathbf{D}_r\mathbf{S}_r + \hat{\mathbf{R}}\mathbf{D}_\theta\mathbf{S}_{r\theta} + \hat{\mathbf{R}}\left(\mathbf{S}_r - \mathbf{S}_\theta\right) = \mathbf{0},\\
&\mathbf{D}_r\mathbf{S}_{r\theta} + \hat{\mathbf{R}}\mathbf{D}_\theta\mathbf{S}_\theta + 2\hat{\mathbf{R}}\mathbf{S}_{r\theta} = \mathbf{0}.
\end{aligned} \tag{66}$$

Thereafter, substituting (65) into (66) results the system equations in matrix form in terms of nodal displacements. For elasticity, the boundary conditions must be considered in (58), where $\beta = r$ and $\theta$ respectively, $t_r$ and $t_\theta$ are tractions along $r$ and $\theta$ directions respectively.

## 6. Numerical examples

*Example 6.1. Infinite plate containing a circular hole under tension $\sigma_0$.*

In this example, a 2D isotropic homogeneous infinite plate containing a circular hole as shown in Figure 6 is observed by meshless method. Due to the symmetry of the problem, only a quarter of plate is modeled. In order to compare the accuracy with analytical solutions for each meshless strategy, the isotropic homogenous medium is considered. The node distribution for $M(=7\times7)$ nodes are presented in both mapped domain and in real domain via mapping/ shape function with infinite element shown in Figure 7(a)(b). The analytical solution of stresses for a circular hole under tensile stress at infinite place is given

$$\begin{aligned}
\sigma_r^* &= \frac{\sigma_0}{2}\left(1-\frac{a^2}{r^2}\right) + \frac{\sigma_0}{2}\cos 2\theta\left(1-\frac{a^2}{r^2}\right)\left(1-3\frac{a^2}{r^2}\right),\\
\sigma_\theta^* &= \frac{\sigma_0}{2}\left(1+\frac{a^2}{r^2}\right) - \frac{\sigma_0}{2}\cos 2\theta\left(1+3\frac{a^2}{r^2}\right),\\
\tau_{r\theta}^* &= -\frac{\sigma_0}{2}\sin 2\theta\left(1-\frac{a^2}{r^2}\right)\left(1+3\frac{a^2}{r^2}\right).
\end{aligned} \tag{67}$$

Because the infinite element cannot be used to model non-zero stress field at infinite in this case, a uniaxial tensile field (particular solution) is added with the principle of superposition in elasticity, i.e.

$$\sigma_r = \frac{\sigma_0}{2}(1+\cos 2\theta)+\sigma_r^{'},\ \sigma_\theta = \frac{\sigma_0}{2}(1-\cos 2\theta)+\sigma_\theta^{'},\ \tau_{r\theta} = -\frac{\sigma_0}{2}\sin 2\theta+\tau_{r\theta}^{'}, \tag{68}$$

where $\sigma_r^{'}, \sigma_\theta^{'}$ and $\tau_{r\theta}^{'}$ are general solutions of stress with zero displacement/stress conditions at infinite. To satisfy the boundary condition of zero tractions on the surface of circular hole, the boundary conditions for general solution are described, when $r = a$, as

$$\sigma_r^0 = -\frac{\sigma_0}{2}(1+\cos 2\theta),\ \tau_{r\theta}^0 = \frac{\sigma_0}{2}\sin 2\theta \quad \text{when } r = a. \tag{69}$$

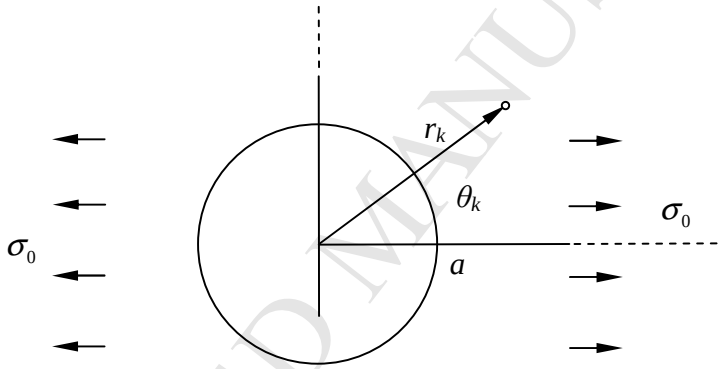


Figure 6. Infinite domain with a circular hole subjected to tensile load $\sigma_0$.

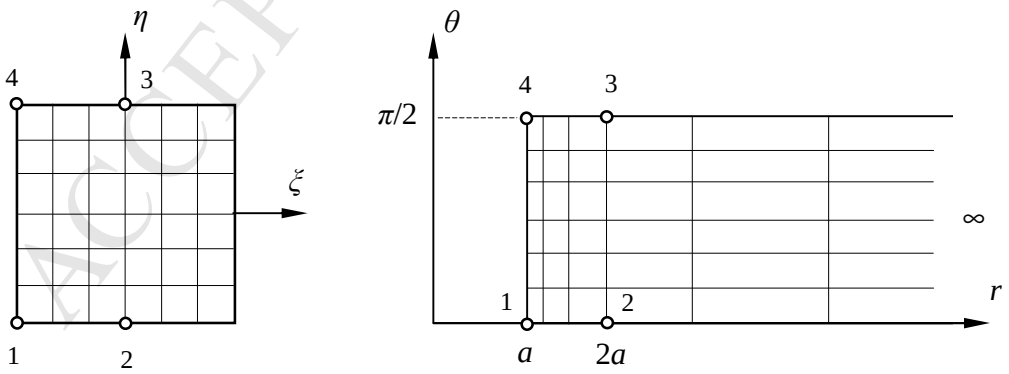


Figure 7. Polar coordinate system: (a) mapped domain; (b) coordinate $(ro\theta)$ with distributed nodes of infinite element.

To show the accuracy for different meshless methods, we consider a regularly distributed collocation points in the mapped domain ($N_\xi = N_\eta$). For both MLS and RBF approaches, the local supported domain is selected as a circle with radius $d_s$ centered at field point ξ, which is determined such that the minimum number of nodes in the sub-domain $n_s \geq 10$. In addition, the number of terms in the complete monomial basis *m* is chosen to 6 for both MLS and RBF methods. The free parameter *c*, in RBF, is chosen as unit in the mapped domain. It has been a big issue how to select the parameter c for long time. The optimal selection has been addressed by Yao et al [41]. However, there is no any free parameter selection using the finite block method. Due to the simplicity of the geometry, only four seeds infinite element is utilised. To investigate the accuracy for different approaches, the average relative errors is defined as

$$\varepsilon = \frac{1}{3M}\sum_{k=1}^{M}\left[\left|\sigma_r(r_k,\theta_k)-\sigma_\theta^*(r_k,\theta_k)\right|+\left|\sigma_\theta(r_k,\theta_k)-\sigma_\theta^*(r_k,\theta_k)\right|+\left|\tau_{r\theta}(r_k,\theta_k)-\tau_{r\theta}^*(r_k,\theta_k)\right|\right]. \quad (70)$$

The numerical results of the average error over all collocation points are shown in Table 1 for different meshless methods vs node density. By observing the results in Table 1, it is clear that the degrees of accuracy for MLS and RBF approaches are very close for each node density. It is also clear that the solution by FBM is much accurate than that either by MLS or RBF method when the node number $N_\xi$ is large than 7. For the sake of analysis convenience in the following examples, only the finite block method is observed combined with infinite element for unbounded media. However, the solutions for FBM will be divergence when $N_\xi$ is large than 20 due to instability of Lagrange series interpolation with uniform distribution of nodes.

Table 1 Average errors $\varepsilon$ for different meshless methods

| $N_\xi$ | MLS | RBF | FBM |
|---|---|---|---|
| 5 | 2.8048e-02 | 6.3232e-02 | 3.4021e-02 |
| 7 | 1.2334e-02 | 2.5512e-02 | 1.7766e-03 |
| 9 | 5.7930e-03 | 1.0258e-02 | 4.6347e-05 |
| 11 | 3.2991e-03 | 4.5900e-03 | 7.3596e-07 |
| 13 | 2.1764e-03 | 2.2970e-03 | 7.7134e-09 |
| 15 | 1.5147e-03 | 1.2679e-03 | 1.2151e-08 |
| 17 | 9.7775e-04 | 7.5231e-04 | 7.7261e-07 |

The effect caused by the truncation of unbounded domain is observed using RBF interpolation with same free parameter selection. The radius of outer boundary $b$ (truncation of boundary) is selected from 4$a$ to 10$a$ and number of node in the domain $N_\xi (= N_\eta)$ is chosen as 11, 19 and 27 respectively. In this case, the distribution of collocation point is also uniform in the mapped domain. Table 2 shows the average errors defined in (70) against the ratio of $b/a$ and the computation effort running on the Lenovo-PC with Intel(R) Processor 5Y70 CPU@1.10GHz. It is clear that the accuracy is improved slightly when the number of node and the radius of domain increase. However, the CPU time in second increases significantly for large number of node. The numerical solutions using RBF with infinite element are listed in the table for comparison. It can be seen that for each number of node selection, the degree of accuracy with infinite element is much higher than that by traditional meshless method with the same level of computation effort. Similar results and conclusions of truncation error and CPU time can be observed using both MLS approach and FBM. Therefore, we can conclude that the infinite element plays a significant role to improve the computational accuracy and efficiency for unbounded medium.

Table 2. Average errors and CPU time for different truncations of unbounded domain.

| $b/a$ | $N_\xi = 11$ | | $N_\xi = 19$ | | $N_\xi = 27$ | |
|---|---|---|---|---|---|---|
| | $\varepsilon$ | CPU(s) | $\varepsilon$ | CPU(s) | $\varepsilon$ | CPU(s) |
| 4.0 | 1.0648e-01 | 6.0000e-01 | 7.8060e-02 | 3.0333e+00 | 7.2835e-02 | 2.5933e+01 |
| 6.0 | 7.6171e-02 | 8.1667e-01 | 4.3334e-02 | 3.2500e+00 | 3.5096e-02 | 2.8417e+01 |
| 8.0 | 6.9144e-02 | 1.0000e-01 | 3.5701e-02 | 3.1333e+00 | 2.5413e-02 | 3.0850e+01 |
| 10.0 | 6.6478e-02 | 7.8333e-01 | 3.3752e-02 | 3.8667e+00 | 2.2349e-02 | 2.9983e+01 |
| Infinite | 4.5900e-03 | 8.1667e-01 | 4.7377e-04 | 3.5500e+00 | 1.2650e-04 | 3.0617e+01 |

*Example 6.2. Infinite strip containing a circular hole under tensile load* $\sigma_0$.

Firstly consider an isotropic homogeneous infinite strip containing a circular hole under a uniaxial load $\sigma_0$. Again, only a quarter of plate is modeled as the symmetry with two 8-seeds blocks and one 5-seeds finite element shown in Figure 8. To catch up the stress concentration accurately, the coordinates of node in mapped domain is selected to be Chebyshev's roots, as

$$\xi_k = \cos\frac{\pi(k-1)}{N_\xi},\quad k = 1,2,...,(N_\xi+1),\ \eta_l = \cos\frac{\pi(l-1)}{N_\eta},\quad l = 1,2,...,(N_\eta+1) \tag{71}$$

and the distribution of node in real domain is shown in Figure 9 in the case of $N_\xi = N_\eta = 14$. The analytical solution of maximum stress at point A is given as $\sigma_{\max} = K\sigma_0 w/(w-a)$ [42], where *K* defined as the stress concentration factor is given by

$$K = 3.00 - 3.13\left(\frac{a}{w}\right) + 3.66\left(\frac{a}{w}\right)^2 - 1.53\left(\frac{a}{w}\right)^3. \tag{72}$$

Numerical solutions of concentration factor *K* obtained by using FBM are presented in Figure 10 versus the ratio of radius of the circular hole *a* and the half width of the strip *w*. Analytical solutions are presented in the same figure for comparison and excellent accuracy is observed.

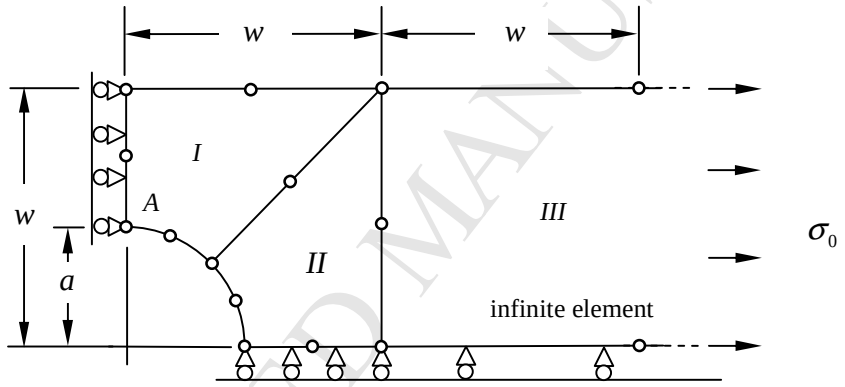


Figurer 8. A quarter of infinite strip containing circular hole with two blocks and one infinite element.

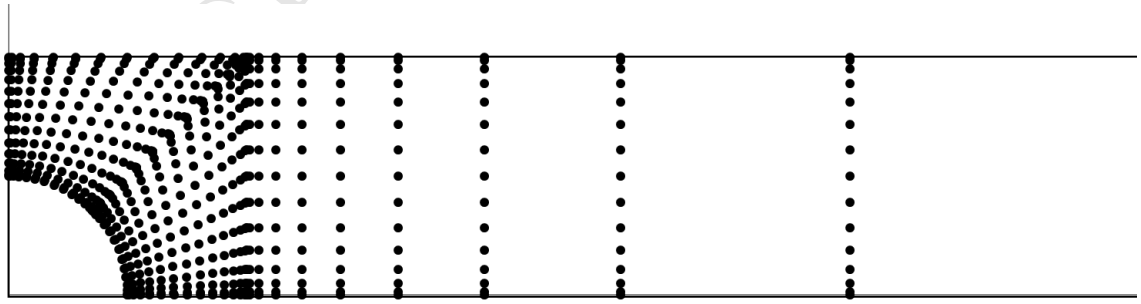

Figure 9. Nodal distribution in the physical domain: two blocks and one infinite element.

Secondly, consider an infinite strip containing a circular hole with functionally graded material. In this example, a non-homogenous functionally graded material is considered and the elastic modulus has an exponential variation in *y*-axis as $E = E_0 f(y)$, where $f(y) = e^{\alpha|y|}$, $\alpha$ is arbitrary constant and $E_0$ is elastic modulus on the bottom. In engineering, it represents an infinite strip bonded with two strips of FGM. The Poisson ratio $\nu = 0.3$ and shear modulus $G(y) = E(y)/2(1+\nu)$. Plane stress is assumed. The particular solution can be obtained by considering a constant uniaxial strain $\varepsilon_x^0$ in a strip without hole. By using Saint-Venant's Principle, the stresses in domain are

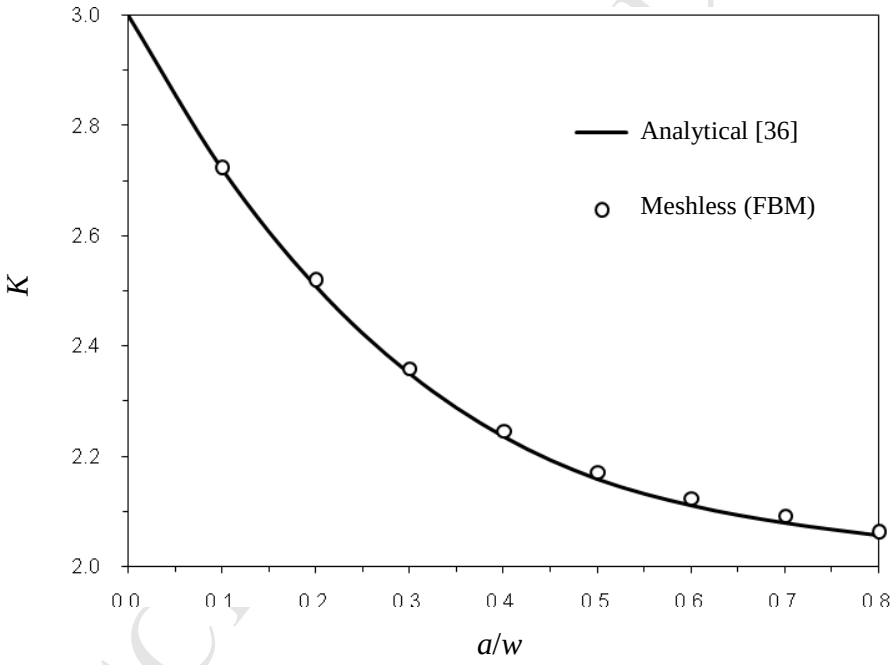


` Figure 10. Stress concentration factor *K* for a strip with circular hole.

$$\sigma_x = \beta E \varepsilon_x^0,\ \sigma_y = 0,\ \tau_{xy} = 0, \tag{73}$$

where coefficient $\beta$ can be determined by considering equivalency as

$$\int_0^w \sigma_x dx = \sigma_0 w, \tag{74}$$

which gives $\beta = \dfrac{\alpha w \sigma_0}{(e^{\alpha w}-1)E_0}$. Therefore, one has general solution of stresses

$$\sigma_x = \alpha w \sigma_0 e^{\alpha y}/(e^{\alpha w}-1) + \sigma_x^{'},\ \sigma_y = \sigma_y^{'},\ \tau_{xy} = \tau_{r\theta}^{'}. \tag{75}$$

In the Cartesian coordinate system, the traction boundary conditions on the hole hold

$$t_x^0 = -\alpha h \sigma_0 e^{\alpha a \sin\theta}\cos\theta/(e^{\alpha w}-1),\ t_y^0 = 0. \tag{76}$$

where $\theta = \text{atan}(y/x)$. The stress distributions $\sigma_x$ and $\sigma_y$ along $y$-axis when $x = 0$ in and $a/w = 0.5$ are shown in Figure 11 and 12 respectively for different coefficient $\alpha$. The numerical solutions given by FEM (ABAQUS) [43] are also presented in the figures to demonstrate the agreement.

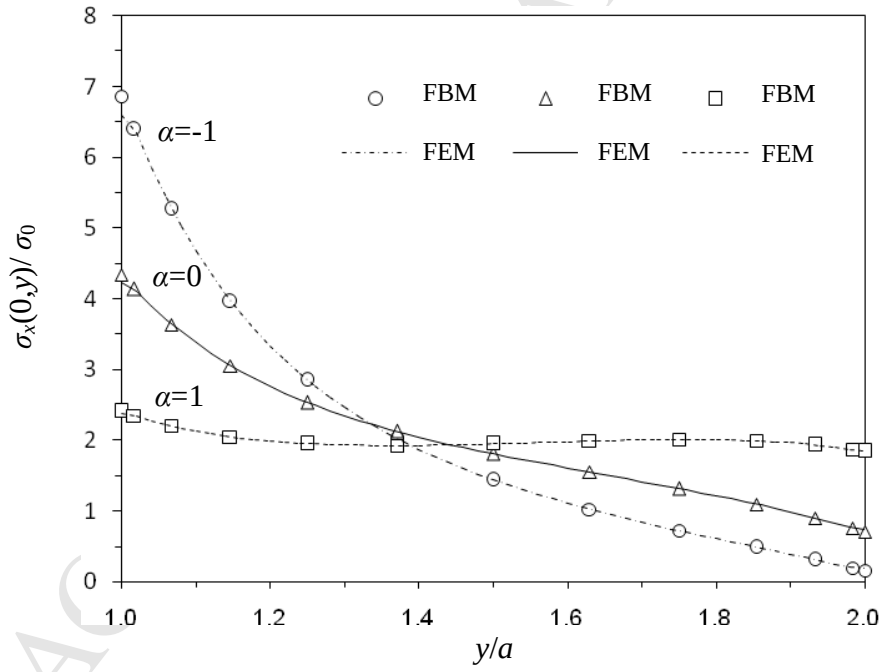


Figure 11. Distribution of normal stress $\sigma_x(0, y)$.

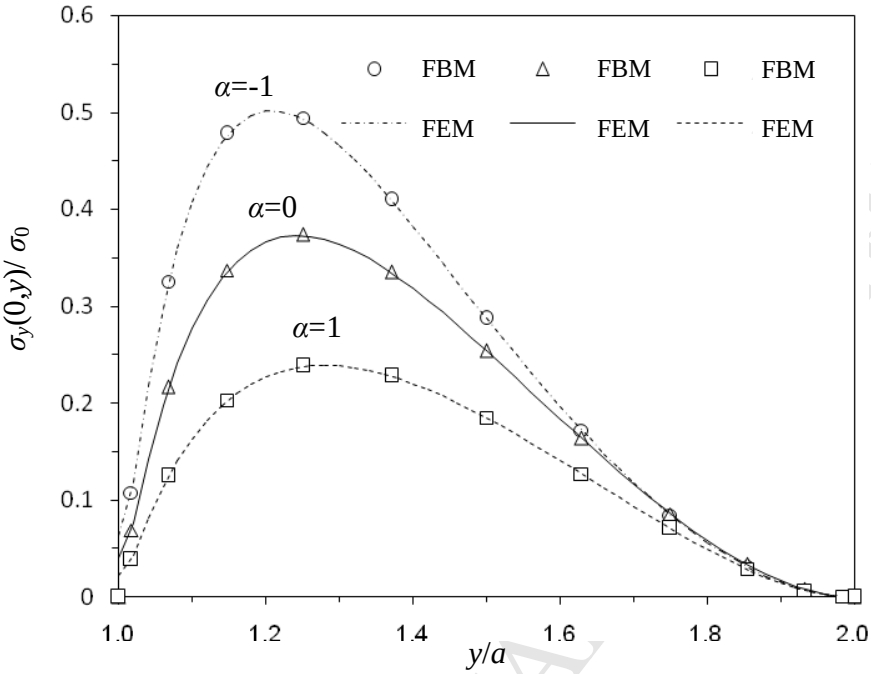


Figure 12. Distribution of normal stress $\sigma_y(0, y)$.

*6.3. Cracked infinite strip under tension* $\sigma_0$.

For a cracked strip, four blocks are needed to model crack problem as shown in Figure 13. For non-homogeneous linear elastic solids, Eischen [44] showed that the asymptotic crack-tip stress and displacement fields have the same form as those in homogeneous linear elastic materials. Therefore, for isotropic FGM plane stress case, the mixed mode stress intensity factors are obtained from

$$K_{\mathrm{I}} = \frac{\sqrt{\pi a}\Delta u_{\mathrm{I}}}{4E_{\mathrm{tip}}\sqrt{2r}},\quad K_{\mathrm{II}} = \frac{\sqrt{\pi a}\Delta u_{\mathrm{II}}}{4E_{\mathrm{tip}}\sqrt{2r}}, \tag{77}$$

where $\Delta u_{\mathrm{I}}$ and $\Delta u_{\mathrm{II}}$ are relative opening and shearing crack displacements, $E_{\mathrm{tip}}$ is Young's modulus at crack tip and $r$ is the distance measured from crack tip. Firstly Consider an infinite strip of width $w$ with a central crack of length $2a$ subjected to a uniform tensile load $\sigma_0$ at infinite.as shown in Figure 13. Because of the singularity of the stresses at the crack tip, the nodal distribution in the normalised domain is selected to be Chebyshev's roots in (71) with nodal density $N_\xi = N_\eta = 21$ for each block and infinite element. The convergent numerical

solutions can be obtained when $N_\xi = N_\eta \geq 15$. The numerical results of the normalised stress intensity factors $K_I / \sigma_0 \sqrt{\pi a}$ versus the ratio of $a/w$ are plotted in Figure 14, where the distance $r/a = 0.09549$ (location of the fourth node from the crack tip). In the case of $a/w$=0.1 or 0.9, the relative error is about 4% due to the difference of the size effect between block I and II.

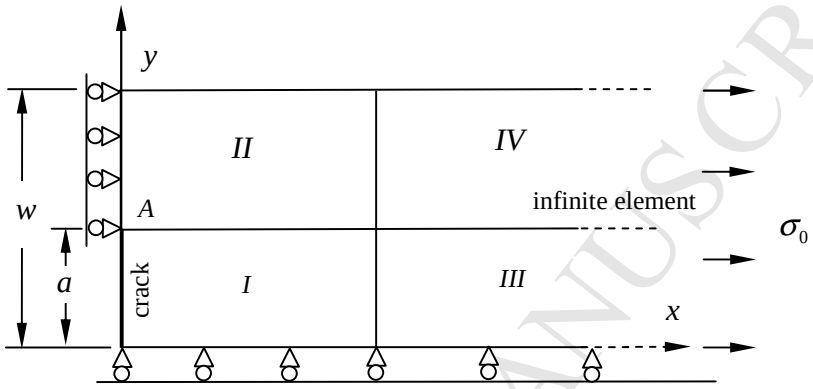


Figure 13. Central cracked infinite strip subjected to a tensile load.

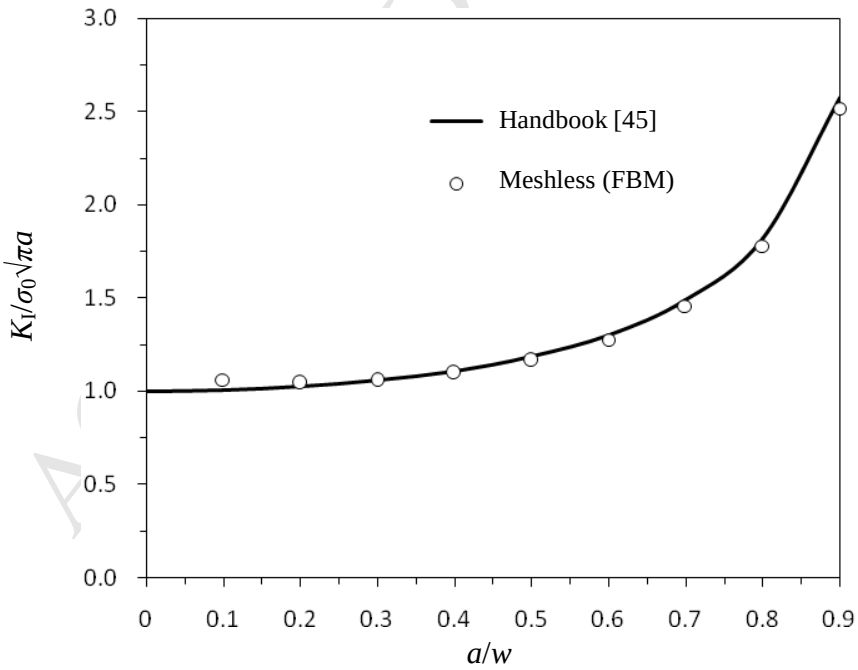


Figure 14. Normalized stress intensity factor versus the ratio of $a/w$.

Next, non-homogenous material with an edge crack shown in Figure 15 is considered and the elastic modulus has an exponential variation along *y*-axis as $E(y)=E_0 f(y)$ , where $f(y)=e^{\alpha y/w}$ and $\alpha$ is dimensionless constant and defined as $\alpha=\ln(E_w/E_0)$ , $E_0$ and $E_w$ are Young's moduli on the bottom and top layers of the strip respectively. Shear modulus $G(y)=E(y)/2(1+\nu)$ and Poisson ratio $\nu=0.3$. In order to obtain the particular solution for an infinite long strip without crack subjected to either uniform tensile load *P* or bending moment $M$ , the normal strain can be written, from plane assumption, as

$$\varepsilon_x=\varepsilon_0+\varphi_0 y, \tag{78}$$

where $\varepsilon_0$ and $\varphi_0$ are two constants. The solution of stress is given

$$\sigma_x=(\varepsilon_0+\varphi_0 y)E_0 e^{\alpha y/w}, \sigma_y=\tau_{xy}=0 \tag{79}$$

By using Saint-Venant's Principle, the equivalent traction boundary conditions become

$$\int_0^w \sigma_x dy=P,\ \int_0^w \sigma_x y dy=-M+\frac{Pw}{2}, \tag{80}$$

where $P=\sigma_0 w$ and *M* is bending moment at the infinite. Substituting (79) into (80) and solving linear algebraic equations yields

$$\varepsilon_0=\frac{PI_2-(-M+Pw/2)I_1}{I_0I_2-I_1^2},\ \varphi_0=-\frac{PI_1-(-M+Pw/2)I_0}{I_0I_2-I_1^2}, \tag{81}$$

where $I_k=\int_0^w y^k e^{\alpha y/w}dy$ and

$$I_0=\frac{w}{\alpha}(e^{\alpha}-1),\ I_1=\frac{w^2}{\alpha^2}[1+e^{\alpha}(\alpha-1)],\ I_2=\frac{w^3}{\alpha^3}[-2+e^{\alpha}(\alpha^2-2\alpha+2)]. \tag{82}$$

To demonstrate the accuracy of meshless method with infinite element, a cracked strip with the ratio $a/w=0.5$ is observed. For the case under a pure bending moment, the applied stress $\sigma_0=6M/w^2$ from plate bending theory. The normalised stress intensity factors $K_I/\sigma_0\sqrt{\pi a}$ under tensile and bending loads are presented in Table 3 versus different ratio of material properties $E_w/E_0$. Agreement of numerical solution by meshless method (FBM) with either analytical solutions by Erdogan and Wu [46] or FEM by Kim and Paulino [47] for long strip

($L = 4w$) are demonstrated in Table 3. It is reasonable that the stress intensity factor for infinite cracked strip is smaller than that for finite strip.

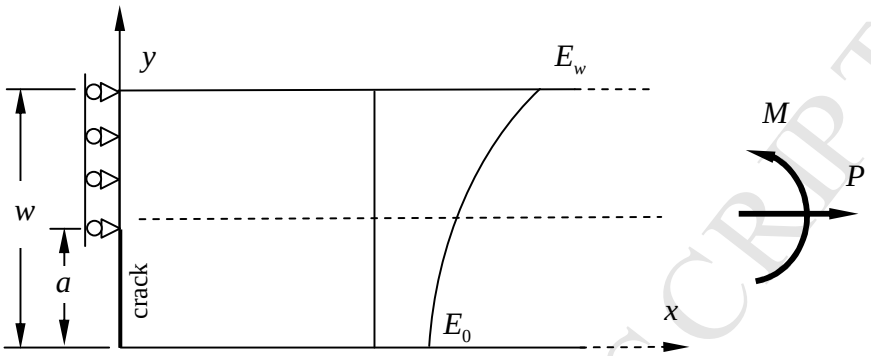


Figure15. Edge cracked strip under tensile load and bending moment in FGM.

Table 3. Normalized SIF $K_I / \sigma_0 \sqrt{\pi a}$ for edge cracked strip.

| | $E_w / E_0$ | FBM | Erdogan [46] | Kim [47] |
|---|---|---|---|---|
| Tensile | 0.1 | 3.4220 | 3.570 | 3.496 |
| | 0.2 | 3.2159 | 3.326 | 3.292 |
| | 1 | 2.7159 | NA | 2.822 |
| | 5 | 2.2330 | 2.365 | 2.366 |
| | 10 | 2.0310 | 2.223 | 2.175 |
| Bending | 0.1 | 2.1196 | 2.215 | 2.145 |
| | 0.2 | 1.9015 | 1.953 | 1.925 |
| | 1 | 1.4567 | NA | 1.496 |
| | 5 | 1.1047 | 1.151 | 1.158 |
| | 10 | 0.9750 | 1.035 | 1.035 |

## 7. Conclusion

The Meshless approaches, including moving last square method, radial bases function method and finite block method, combined with infinite element was presented in this paper for general linear elasticity of two dimensional problems with unbounded media. Mapping a infinite domain into an normalised domain with infinite element, the system equations in a strong form are formulated with the first order partial differential matrices from the equilibrium

equations and boundary conditions. Comparisons between these meshless methods with different interpolations have been made and show that the finite block method with Lagrange series in the mapping domain is of highest accuracy. Apart from all advantages of meshless method, the finite block method is of much higher accuracy and convergence degrees. For complicated large scale dimension problems, only few blocks are needed in the domain. Therefore it is much easier to handle few blocks with certain domain collocation points. This method can be extended easily to any types of partial differential equations, including nonlinear problem etc with unbounded media. The presented method can also be combined with other methods such as finite element method and boundary element method directly.

## Acknowledgement

The authors would like to thank the support from the National Natural Science Foundation of China (No.51478053, No. 11601528.)

## References

[1] Zienkiewicz OC, Kelly DW, Bettess P. The coupling of the finite element method and boundary solution procedures. *Int. J. Numer. Methods Eng*. 1977; 11: 355-375.

[2] Brebbia C, Walker S. *Boundary element techniques in engineering*, Newnes Butterworths, London, England, 1980.

[3] Wood WL. On the finite element solution of an exterior boundary value problem. *Int. J. Numer. Methods Eng.* 1976; 10: 885-891.

[4] Bettess P, Zienkiewicz OC. Diffraction and refraction of surface waves using finite and infinite elements. *Int. J. Numer. Methods Eng.* 1977; 11: 1271-1290.

[5] Khalili N, Valliappan S, Tabatabaie Yazdi J, Yazdchi M. 1D infinite element for dynamic problems in saturated porous media. *Commu. on Numer. Methods in Eng.* 1997; 13: 727-738.

[6] Zienkiewicz OC, Emson C, Bettess P. A novel boundary infinite element. *Int. J. Numer. Methods Eng*.1983; 19: 393-404.

[7] Selvadurai APS, Karpurapu R. Composite infinite element for modeling unbounded saturated-soil media. *J Geotech. Geoenviro. Eng.* 1989; 115: 1633-1646.

[8] Bettess P. *Infinite Elements*. Penshaw Press, Sunderland, UK, 1992.

[9] Bettess P. Infinite elements. *Int. J. Numer. Methods Eng.* 1977; 11: 53-64.

[10] Damjanic F, Owen DRJ. Mapped infinite element in transient thermal analysis. *Computers & Structures* 1984; 19: 673-687.

[11] Zienkiewicz OC, Bando K, Bettess P, Emson C, Chiam TC. 1985. Mapped infinite element for exterior wave problems. *Int. J. Numer. Methods Eng.* 1985; 21: 1229-1251.

[12] Simoni L, Schrefler BA. Mapped infinite elements in soil consolidation. *Int. J. Numer. Methods Eng.* 1987; 24: 513-527.

[13] Dong W, Selvadurai APS. A combined finite and infinite element approach for modeling spherically symmetric transient subsurface flow. *Computers & Geosciences* 2009; 35: 438-445.

[14] Marques JMMC. *Finite and infinite elements in static and dynamic structural analysis*. PhD Thesis, University of Wales, 1984.

[15] Gingold RA, Monaghan JJ. Smoothed Particle Hydrodynamics: theory and application to non-spherical stars. Mon. Notices R. Astro. Soc. 1977; 181: 375–389.

[16] Lucy BL. A Numerical Approach to Testing the Fission Hypothesis. *Astron. J.* 1977; 82 (12); 1013–1924.

[17] Liu GR. *Mesh Free Methods Moving beyond the finite element Method.* USA: CRC Press, 2003.

[18] Nayroles B, Touzot G, Villon P. Generalizing the finite element method: diffuse approximation and diffuse elements. *Computational Mechanics* 1992; 10: 307-318.

[19] Belytschko T, Lu YY, Gu L. Element-free Galerkin method. *Int. J. Numer. Methods Eng.*1994; 37: 229-256.

[20] Liu WK, Jun S, Zhang Y. Reproducing kernel particle methods. *Int. J. Numer. Methods Eng.* 1995; 20: 1081-1106.

[21] S.N. Atluri & T. Zhu, A new meshless local Peyrov-Galerkin (MLPG) approach to nonlinear problems in computational modelling and simulation, *Comput Model Simul Engng*, **3**, 187-196, 1998.

[22] S.N. Atluri & T. Zhu, A new meshless local Peyrov-Galerkin (MLPG) approach in computational mechanics, *Comput Mech*, **22**, 117-127, 1998.

[23] S.N. Atluri & T. Zhu, The meshlesss local Peyrov-Galerkin (MLPG) approach for sovling problems in elasto-statics, *Comput Mech*, **25**, 169-179, 1999.

[24] S.N. Atluri & S. Shen, The meshlesss local Peyrov-Galerkin (MLPG) method: a simple and less-costly alternative to the finite element and boundary element method, *Comput Model Engng Sci*, **3**, 11-52, 2002.

[25] S.N. Atluri, *The Meshless Method (MLPG) for Domain and BIE Discretizations*, Forsyth, GA, USA, Tech Science Press, 2004.

[26] J. Sladek, V. Sladek & Ch. Zhang, Heat conduction analysis in nonhomogeneous anisotropic solid, ZH Yao, MW Yuan, WX Zhong edited, Computational Mechanics, Tsinghua University Press and Springer, 609-614, 2004.

[27] J. Sladek, V. Sladek & S.N. Atluri, Meshless Local Petrov-Galerkin method for heat conduction problem in an anisotropic medium, *Comput Model Engng Sci*, **6**, 309-318, 2004.

[28] V. Sladek, J. Sladek, M. Tanaka & Ch. Zhang, Local integral equation method for potential problems in functionally graded anisotropic materials, *Engng Analy with Boundary Elements*, **29**, 829-843, 2005.

[29] M.A. Golgerg, C.S. Chen & S.R. Karur, Improved multiquadric approximation for partial differential equations, *Engng Analy with Boundary Elements*, **18**, 9-17, 1996.

[30] R. L. Hardy, Multiquadric equations of topography and other irregular surface, *J. Geophys. Res*., **76**, 1905-1915, 1971.

[31] Y.C. Hon & X.Z. Mao, A multiquadric interpolation method for solving initial value problems, *J. Scientific Computing*, **12**, 51-55, 1997.

[32] Yang J J, Zheng J L. Intervention-point principle of meshless method[J]. *Chinese Science Bulletin*, 2013, 58(4-5):478-485.

[33] Yang J J, Zheng J L. A meshless intervention-point method with h-p-d adaptability. *Applied Mathematics and Mechanics*, 2016, 37(10): 1013-1025.

[34] Yang J J, Zheng J L. Meshless global intervention point (MGIP) method[J]. *Chinese Journal of Applied Mechanics*, 2017, 34(5): 956-962.

[35] Deng YJ, Liu HY and Uhlmann G. On regularized full- and partial-cloaks in acoustic scattering, *Communications in Partial Differential Equations* 2017; 42 (6): 821-851.

[36] Deng YJ, Liu HY and Uhlmann G. Full and partial cloaking in electromagnetic scattering, *Arch. Ration. Mech. Anal*. 2017; 223 (1): 265-299.

[37] Wen PH, Cao P, Korakianitis T. Finite Block Method in elasticity. *Engineering Analysis With Boundary Elements* 2014; 46: 116-125.

[38] Li M, Wen PH. Finite block method for transient heat conduction analysis in functionally graded media. *International Journal For Numerical Methods in Engineering* 2014; 99(5): 372-390.

[39] Li M, Lei M, Munjiza A, Wen PH. Frictional contact analysis of functionally graded materials with Lagrange finite block method. *International Journal For Numerical Methods in Engineering* 2015; 103(6): 391-412.

[40] Li M, Meng LX, Hinneh P, Wen PH. Finite block method for interface cracks. *Engineering Fracture Mechanics* 2016; 156: 25-40

[41] Yao, G, Chen CS, Zheng H. A modified method of approximate particular solutions for solving linear and nonlinear PDEs, *Numerical Methods for Partial Differential Equations* 2017; 33(6): 1839-1858.

[42] Young WC, Budynas RG. *Formulas for Stress and Strain.* McGraw-Hill, New York,2002.

[43] Khennane A. *Introduction to Finite Element Analysis Using MATLAB and Abaqus,* CRC Press, Boca Raton FL, 2013.

[44] Eischen JW. Fracture of non-homogeneous materials . *Int J Fract* 1987; 34:3-22.

[45] Tada H, Paris PC, Irwin GR. *The Stress Analysis of Cracks Handbook*. Del Research Corporation, 1986

[46] Erdogan F, Wu BH. The surface crack problem for a plate with functionally graded properties. ASME *Journal of Applied Mechanics* 1997; 64: 449-456.

[47] Kim JH, Paulino GH. Finite element evaluation of mixed mode stress intensity factors in functionally graded materials. *Int J Numer Meth Eng* 2002; 53: 1903-35.

- Meshless methods with infinite element have been proposed;
- Mapping technique and finite block method are derived;
- Partial differential matrices are obtained by the first order matrix;
- Stress intensity factor for functionally graded materials are determined.